Definition of a unified material model for cellular materials with high morphological and topological dispersion: Application to an AA7075-T6 aluminium foam

Definition of a unified material model for cellular materials with high morphological and topological dispersion: application to an AA7075-T6 aluminium foam

Edoardo Mancini[a,*], Francesca Campana[b], Daniela Pilone[b], Dario Amodio[c] and Marco Sasso[c]

[a]Università degli Studi dell'Aquila, Piazzale Ernesto Pontieri, Monteluco di Roio, I-67100 L'Aquila, Italy

[b]Sapienza Università di Roma, via Eudossiana 18, 00184 Roma, Italy

[c]Università Politecnica delle Marche, via Brecce Bianche, 60100 Ancona, Italy

ABSTRACT

The compression behaviour in quasi-static and dynamic conditions of cellular materials is crucial for their applications both for ensuring structural strength and high energy absorption capability. Despite the recent progress made in understanding the experimental observations, analytical and numerical modelling still requires improvements in the Representative Volume Element (RVE) identification that can be uncertain due to the limited dimensions of the investigated specimens and to the cell inhomogeneity.

The objective of this paper is to implement a material model able to consider the statistical distribution so that its effect can be quantitatively highlighted, mitigating uncertainty of the RVE identification.

The applied methodology started with morphological and topological analyses on samples extracted from an ingot of AA7075T6 foam, which was manufactured by compact powder technology. Quasi-static and dynamic experimental compression tests have been carried out and compared with 3D mesoscale numerical simulations in order to correlate the mechanical behaviour of the foam to the cell characteristics. Finally, an equivalent material model, which is a function of the statistical distributions of cells morphology and topology, has been proposed and analytically verified.

Keywords: cellular material; aluminium foam; SHPB; RVE; high strain rate; homogeneous formulation

* Corresponding author

e-mail address: edoardo.mancini@univaq.it (E. Mancini).

Summary

1 INTRODUCTION 2
2 MATERIALS AND METHODS 5
2.1 Material and sample preparation 5
2.1.1 Base material 7
2.2 Morphological and topological analysis 9
2.3 Experimental equipment 10
2.3.1 Quasi-static test 10
2.3.2 Dynamic tests 11
2.4 Mesoscopic 3D sample generation 13
3 RESULTS AND DISCUSSION 15
3.1 Experimental testing 15
3.1.1 Deformation pattern 18
3.1.2 Fracture surface analysis 21
3.2 Morphological and topological analysis results 21
3.3 Numerical simulation results 24
3.4 Model definition and calibration on AA7075-T6 foam 28
4 CONCLUSIONS 32
5 DATA AVAILABILITY 33
6 REFERENCES 33

1 INTRODUCTION

Metallic foams are cellular materials similar to the natural ones that have a bulk matrix with a large number of voids, also named cells. Differently from porous materials which are characterized by isolated pores and relatively low porosity ($\varphi < 70\%$), foams are characterised by a very high porosity ($70\% < \varphi < 99.7\%$) leading to a much lower density than that of the base material [1]. Cellular materials are classified according to their cell morphology and topology. Cells are open or closed, connected by sharing struts (edges of open cells) or walls (faces and edges of closed cells). They exist since 1956 [2] and can be manufactured with different types of materials, including metals, polymers, ceramics, composites, etc. The interest in their use increased with the development of less expensive processing techniques such as foams produced from liquid or solid metal powders and from vapour or gaseous metals or metal ions [3][4].

Cellular materials are, in general, interesting for many engineering applications due to their mechanical, thermal, acoustic and electromagnetic properties [5][6]; aluminium used as bulk material for cellular structure answered to an increasing demand for realizing lightweight structures with good structural resistance and for producing energy absorption devices.

Their importance is still growing in transportation, aerospace, defence, building and biomedical industries; the transportation and especially the automotive sector are interested in the use of aluminium foams both as structural materials and as energy absorbers [1][3][5]. If they are used as energy absorber or to mitigate impact loads, their compressive proprieties both in quasi-static and dynamic conditions, should have isotropic mechanical properties and flow stress-strain curves characterized by a stress plateau after yielding. The presence of this plateau allows them to absorb considerable quantity of energy by plastic dissipation due to large deformations at nearly constant nominal stress [7][8][9].

Metallic foams are attractive materials for crashworthiness design, where loads and material responses have to be investigated in dynamic conditions. Nevertheless, due to the difficulty of identifying the strain rate effect on the deformation behaviour of foams, conflicting results can be found in literature. Furthermore, metallic foams made by powder technology are characterised by the presence of stochastic closed cells. The related inhomogeneity emphasizes the scattering of results both in terms of stress–strain curves and maximum strength. This scattering is attributed to relative density fluctuation (e.g., global cell distribution, isolated large cells) and to base material microstructure and defects. Deshpande and Fleck [9] highlighted how cellular materials like aluminium foams are highly heterogeneous and have considerable scatters of compressive properties, defining the strain-rate sensitivity of the alloy behaviour only when the increase in dynamic strength is larger than the scatter band (20% adopted [9]). The scatter of compressive properties was detected also in other works where the authors pointed out that a sufficient number of tests at different strain-rates should be carried out in order to evaluate both the average values of the mechanical properties and the standard deviation [10][11]. However, it is noteworthy how a fundamental role is played by the specimen size in terms of its representativeness of the studied cellular material for predicting its effective properties. Indeed, the first important issue in mechanical testing of foams is the effect of the specimen size, relative to the cell size, on the measured properties. This has led to refer to a sample as the Representative Volume Element (RVE). Formerly defined by Hill in 1963 [12] now it is widely accepted. E.W. Andrews et al [13] before and C. Tekoğlu et al [14] later pointed out that tested samples without a sufficient number of cells are not representative of the studied material properties because

of relevant size effect. As a matter of fact, local density variations play an important role in determining the strength variability. C. Redenbach et al. [15] by using the concept of statistical volume elements (SVE) confirmed that the size of the RVE increases with increasing cell size variation. Moreover, size effects are likely to appear when the RVE size and the cell size are of the same order. L. Li et al [16] proposed a method, based on a statistical analysis of cell geometrical parameters, to establish the relationship between microstructural parameters and the macro-structure of foams. They pointed out the effect of cell size on Young modulus and plateau stress and they concluded saying that cell size has little effect on eventual dynamic strength increase when the foam base material is independent of strain rate. However, when the base material is dependent on strain rate, foams with a large number of small cells exhibit higher dynamic stress. The stress plateau stage has been found to be very sensitive to stain rate by several authors, while other authors demonstrated that the effect of strain rate could be ignored [11][17][18]. This discrepancy has been investigated and attributed to the interaction between strain rate effect (local and global) and inertia effect that seems to be predominant under high-speed impact. Strain rate effects depend on the bulk material properties and on the cell distribution and morphology, while the axial-inertia effect depends on the impact speed and determines a large stress on the front surface that produces a front surface densification zone during deformation [19][11].

For these reasons, a mesoscopic model becomes mandatory to evaluate the mechanical properties of this type of materials (e.g., first peak stress, plateau stress) and to allow the implementation of an equivalent material model for future FE analysis. Furthermore, mesoscopic models are important for identifying mechanisms and quantifying the effects of different small-scale factors (e.g., cell distribution, cell area and roundness) [20]. Doing so, the same mesoscale model of a sample can be used for virtual testing (quasi-static compression, transitional dynamic and shock regimes) [6], allowing the evaluation of cell distribution effects in the respect of experimental samples that are defined with the same nominal characteristics (in particularly this is an issue for stochastic cellular materials having large cells).

The objectives of this paper are to introduce:

- a systematic methodology, supported by numerical mesoscopic models, to evaluate the effects of the cell characteristics on the deviation found in the experimental tests, so that the uncertainty in the identification of the RVE suitable for the experimental tests (quasi-static and dynamic test) may be evaluated and properly compared to analytical (material model chosen) and numerical (cellular structures simulations) observations;

- a procedure for cellular materials model definition with high morphology and topology dispersion useful for the subsequent homogeneous formulation.

The cellular material studied in quasi-static and transitional dynamic conditions in the present work is a metallic closed cell foam made by powder technology (AA7075-T6 aluminium foam; section 2.1) showing strongly dispersed results both in quasi-static condition and at high strain rates (see section 3.1). The dynamic tests have been carried out by means of a direct split Hopkinson bar (see section 2.3.1 and 2.3.2). 3D mesoscopic numerical models have been generated to deeply investigate the experimental evidences. The adopted algorithm generates mesoscopic models with stochastic cell distributions taking into account experimental results of morphology and topology analyses (sections 2.2 and 0). The algorithm uses a Matlab script that implements a random distribution of seeds able to divide the entire volume of the specimen in a 3D Voronoi Diagram that defines the cells (section 2.4). Finally, a model of equivalent material is proposed and analytically verified. Model parameters are identified in relation to the dispersion previously measured by the morphological and topological analysis (see section 3.4).

2 MATERIALS AND METHODS

2.1 MATERIAL AND SAMPLE PREPARATION

The material tested is an AA7075-T6 closed cell foam supplied in small ingots (45x45x100 mm) manufactured by compact powder technology. Specimens have been extracted from one half of the ingot that has been sectioned as shown Figure 1a.

Specimens extracted from ingot part A have been used for static and dynamic compression tests. Regions B-C-D-E have been dissected to obtain specimens for the porosity distribution analyses. Foam ingot was cut by a miter saw minimizing cell wall damage and paying maximum attention to the parallelism of the specimen faces. The operations to obtain the specimens are reported in Figure 1b, *c* and *d*: note that the specimens were extracted from the ingot after removing the external skin (Figure 1c and *d*).

The specimen size was chosen as large as possible (the limitations of the Hopkinson bar have been overcome by adapters) in order to reduce the inhomogeneity effects and to include a sufficient number of cells in all directions. Furthermore, the sample aspect ratios were set to remain within the typical limits suggested for the Hopkinson bar test $0.5 \leq h/a \leq 1$, (where a is maximum cross-sectional length) [21].

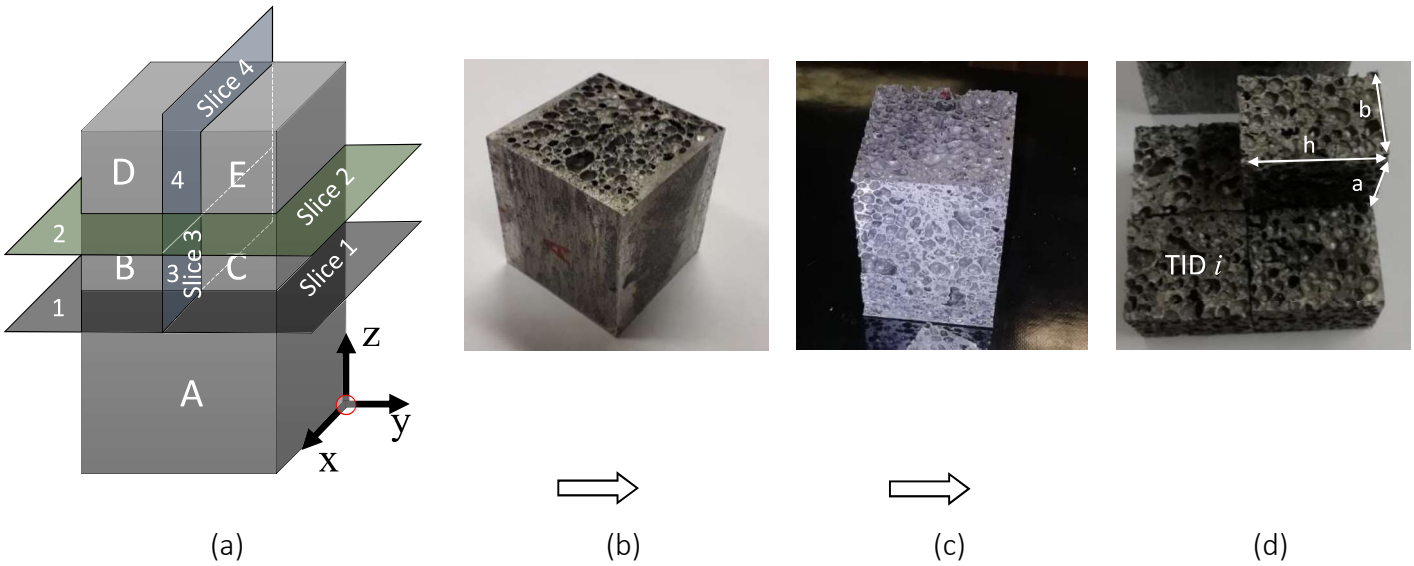

Figure 1. (a) Sketch showing how the ingot has been sectioned (slice 1 to 4), (b) half ingot Part A, (c) Part A without external skin and (d) the obtained specimens.

Mesoscopic structural parameters are mandatory to quantify the cell characteristics which distinguish cellular materials from other engineering materials. Among mesoscopic structural parameters the most important is the relative density [1], which indicates the percentage of solid content in the cell structure and is defined as

$$\rho_{rel} = \frac{\rho_{eff}}{\rho_{bulk}} = 1 - \varphi \qquad (1)$$

where ρ_{eff} is the foam density, ρ_{bulk}, is the density of base material (AA7075 aluminium in the present paper), and φ is the porosity. Other important parameters are the cell morphology (size, shape, orientation, wall/strut thickness) and topology (open or closed, connectivity, distribution). These parameters have been measured and they will be detailed in the sections 2.2 and 3.1.2.

The samples tested in quasi-static and dynamic conditions are listed in Table 1. The relative and effective density, ρ_{eff}, are reported too. The QS 2 sample was cut in a wrong way leading a lower relative density. It was considered as an outlier for the ρ_{rel} evaluation. The ingot without external skin was evaluated too (Figure 1c). It has a relative density of ~0.3.

Table 1. Specimen for quasi-static and dynamic tests

TID#	Type	a (mm)	b (mm)	h (mm)	ρ_{eff} (kg/m^3)	ρ_{eff}/ρ_{Al}
1	QS	18.81	18.12	22.15	722.5	0.268
2		18.57	17.65	18.86	517.2	0.192
1	Dyn	18.19	18.03	22.82	735.6	0.272
2		18.15	17.93	21.61	769.0	0.285
3		18.95	17.87	23.07	664.9	0.246
4		18.83	17.95	22.62	607.2	0.225
5		18.87	17.82	22.50	743.3	0.275
				Mean	**707.1**	**0.262**
				Std. dev.	**54.7**	**0.020**

2.1.1 Base material

The base material used for fabricating the cellular component can be significantly influenced, in term of strain-rate sensitivity, by the alloy composition and microstructure[22][23]. Moreover, the manufacturing process can emphasize the differences between the mechanical properties of the base alloy and those of the alloy that constitutes the cell walls. This can be ascribed to the presence of elements coming from the foam production process, like titanium, and to the presence of intermetallic compounds, precipitates, shrinkage cavities and pores. They generate microscopic heterogeneities, as observed in many aluminium foams, that can lead to mechanical properties significantly different from the base material [24,25].

In order to characterise the base material and to determine the alloy temper state, micro-hardness tests have been carried out on the foam cell walls. The hardness measured value (160 HV) revealed that the alloy has been subjected to aging and the mechanical property values obtained from the authors in [26] for the AA7075 T6 alloy were taken into consideration. The mechanical property values reported in Table 2 are the ones selected for simulations.

Table 2. Vickers micro-hardness and mechanical proprieties

Material	HV	E [GPa]	R_s [MPa]	R_m [MPa]	A %
AA7075-T6	160	72	435	505	13

Some specimens after cutting, grinding, polishing and etching with the Keller's reagent, have been inspected by means of SEM/EDS in order to characterise composition and microstructure of the AA7075 alloy. EDS analyses highlighted that the base alloy is an AA7075 alloy, although it contains 8.6 % Zn and 2.3% Cu that are slightly above the composition limit, and 1.1 % Mg, which is below the composition limits. Figure 2 shows the microstructure of the alloy. As it can be observed in this figure, the alloy is characterized by the presence of microcavities and the microstructure shows the presence of a dendritic structure with interdendritic areas richer in Mg, Cu and Zn. It is well known from the literature that below the solidus temperature, four major intermetallic phases can occur in Al–Zn–Mg–Cu alloys: $\eta(MgZn_2)$, $T(Al_2Mg_3Zn_3)$, $S(Al_2CuMg)$ and $\theta(Al_2Cu)$. Whilst, copper is soluble in η and T phases, θ and S phases are binary and ternary phases in the Al–Cu and Al–Cu–Mg systems, respectively [27][28]. A close observation of the alloy microstructure shows that the interdendritic area presents both fine interdendritic and coarse secondary phases. The presence of coarse secondary phases and Ti particles can deeply affect the fracture toughness of the alloy, by increasing its brittleness. It must be also considered that shrinkage cavities and pores act as stress intensifiers by favouring propagation of cracks. By observing Figure 2 it is possible to see the presence of big cavities in the cell walls ((a) and (b)). The formation of these cavities is ascribable to the lack of liquid metal that, during solidification, should compensate for the alloy shrinkage: in fact, the presence of hydrogen bubbles hinders liquid metal feeding during solidification. SEM micrographs in Figure 2c and Figure 2d highlight the presence of shrinkage cavities with well evident dendrite branches and small round cavities due to gas evolution.

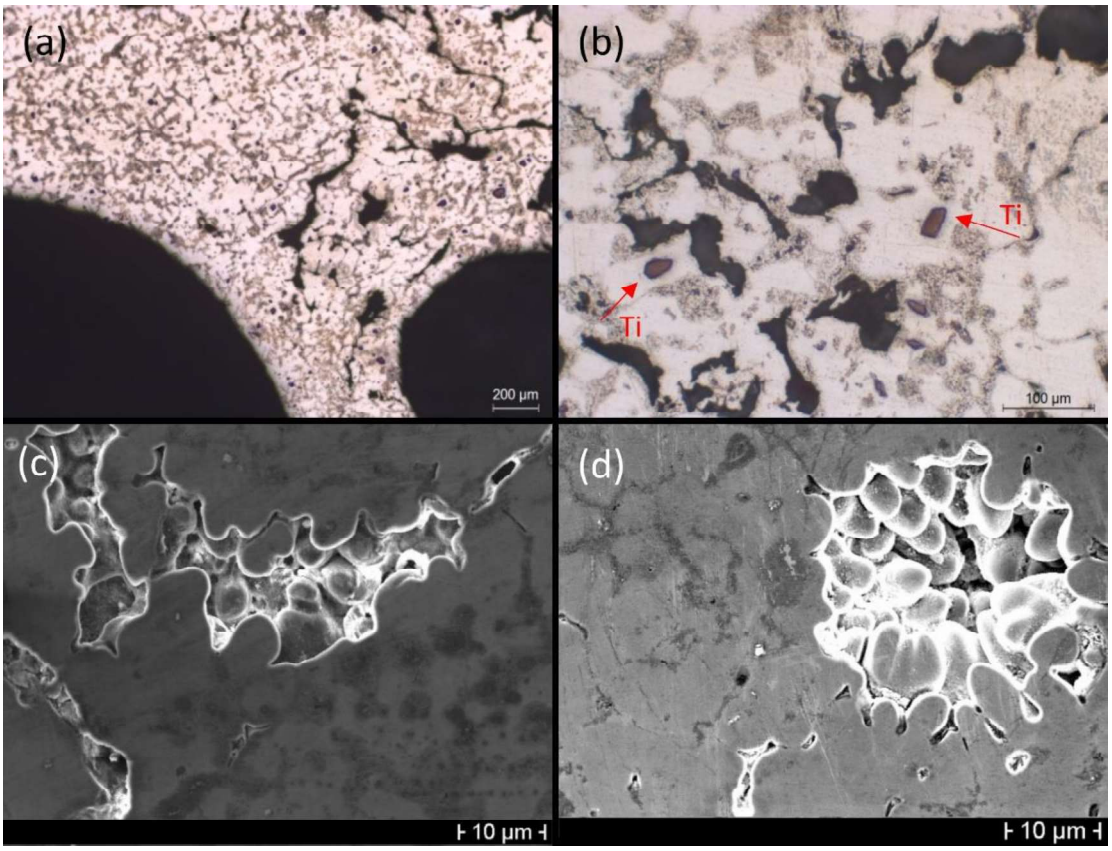

Figure 2. Optical micrographs showing the alloy microstructure at lower magnification (a) and at higher magnification (b): Ti particles and interdendritic areas are well visible, while the black areas are shrinkage cavities and pores (rounded cavities). SEM micrographs (c) and (d) show details of shrinkage cavities with well visible dendrite tips and rounded gas cavities.

2.2 MORPHOLOGICAL AND TOPOLOGICAL ANALYSIS

Considering that size and morphology of cells strongly affect the foam behaviour, the morphological analysis of the foam could be of paramount importance for understanding the foam mechanical response. As already described in section 2.1 the ingot has been sectioned and, after grinding and polishing, macrographs of the different sections have been taken in order to perform image analysis by means of Leica Application Suite®.

After pre-processing of the image to remove the noise and after improving it, the regions of interest have been highlighted for feature determination [29]. The average void density and cell roundness were determined for every considered area in order to evaluate a possible correlation between cell shape irregularity and its position along the specimen. Void density (D_v) is given by:

$$D_v(\%) = \frac{\sum A_i}{A_{tot}} * 100 \qquad (2)$$

where A_i stands for the i_{th} void area and A_{tot} stands for the investigated total area.

Cell roundness (R) gives indications about the morphological characteristic of cavities. It is a non-dimensional parameter defined by:

$$R = \frac{L^2}{4\pi A_i * 1.064} \quad (3)$$

where *L* is the cell perimeter and 1.064 is a factor that takes into consideration the error made in the area calculation by the digitalization of the image, during which continuous perimeters are approximated by discrete rectangles. *R* is equal to 1 when the shape of the considered region is circular, while *R*-values greater than 1 characterize voids that differ from circles.

2.3 EXPERIMENTAL EQUIPMENT

2.3.1 Quasi-static test

A universal electro-mechanical test machine (Zwick/Roell Z050) was used to carry out experimental compression tests in quasi-static conditions. The tests have been conducted in displacement control, at constant engineering strain rate of 10^{-3} s^{-1}. The tool/specimen interfaces were lubricated with MoS2 grease (Molykotes BR-2) to reduce friction; the same lubricant was also used in the dynamic tests. Because of the irregular edges of the foam as well as the isolated larger cells the problems associated with the mounting and the stability of the extensometer have been overcome mounting it on two cylindrical spacers placed above and below the specimen. Quasi-static facility set up is shown in Figure 3. In the enlarged picture on the right, it is possible to see the sample before and after the test.

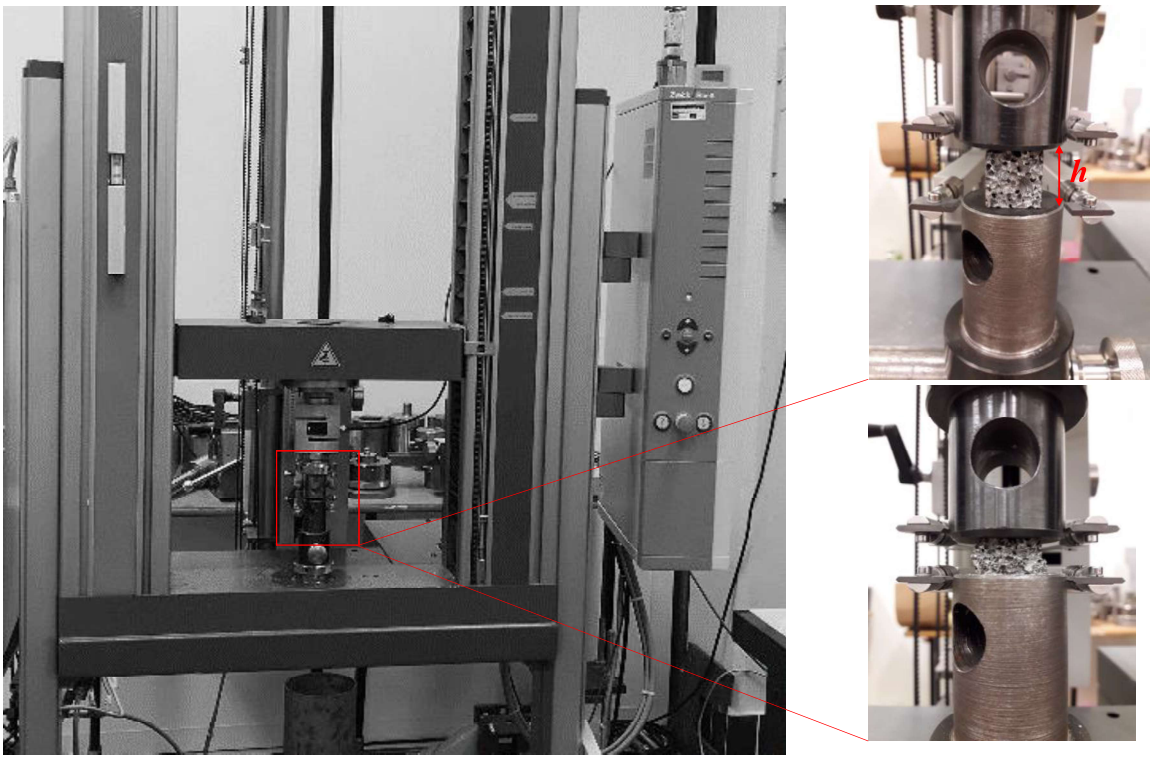

Figure 3. Quasi-static test set-up

2.3.2 Dynamic tests

The dynamic tests have been carried out by means of the Split Hopkinson Bar (SHB) available at Polytechnic University of Marche [30][31]. SHB is the most commonly used apparatus for dynamic testing engineering materials [32][21].

The configuration adopted for this apparatus consists of three aligned bars (Figure 4 and Figure 5a), respectively 3 m (*pre-stressed*), 7.5 m (*input bar*) and 4 m (*output bar*) in length; the bars are made of 17-4PH steel and have a diameter of 18 mm. The specimen, placed between the input and output bars, is deformed by elastic pressure wave that travels in the bars. The wave is generated by pre-loading part of the input bar, commonly named pre-stressed bar, and by suddenly releasing it. The wave travels along the input bar (*incident wave*) at the sound speed of the bar material: as the wave reaches the specimen, the latter is quickly deformed; at the bar-specimen interface the wave is partially reflected back into the input bar (*reflected wave*) and partially transmitted to the output bar (*transmitted wave*) across the specimen itself (Figure 4). The bars are designed to remain in their elastic field while the sample undergoes large strain.

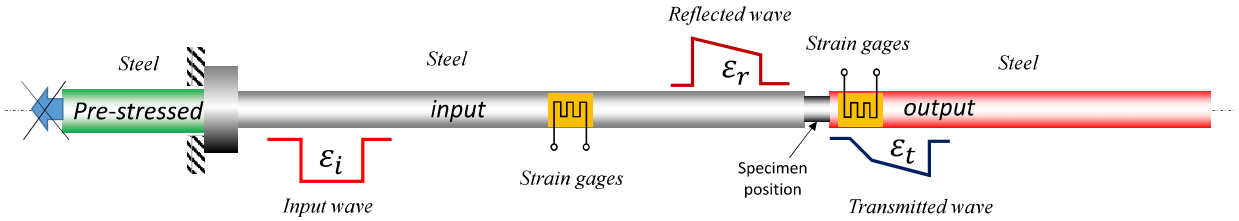

Figure 4. Direct SHB schematization

By means of strain gage rosettes properly placed on the input and output bars, it is possible to measure the strain induced by the incident $\varepsilon_i(t)$, reflected $\varepsilon_r(t)$ and transmitted $\varepsilon_t(t)$ waves. Then, in the hypothesis that the sample deforms uniformly and is in dynamic equilibrium, the engineering strain rate, strain and stress experimented by the sample can be obtained from the classical ''reduced'' formulae:

$$\dot{\varepsilon(t)} = -\frac{2C_0}{L_S}\varepsilon_r(t) \quad (4)$$

$$\varepsilon(t) = -\frac{2C_0}{L_S}\int_0^t \varepsilon_r(t)dt \quad (5)$$

$$\sigma(t) = \frac{A_b E_b}{A_S}\varepsilon_t(t) \quad (6)$$

where L_s and A_s represent the initial height and cross-sectional area of the sample, respectively; C_0, E_b and A_b indicate the sound speed, the elastic modulus and the cross-sectional area of the bars. Synchronizing the reflected and transmitted signals, the flow stress–strain of the material at high strain rate is obtained.

All tests have been recorded by a FastCam (Photron® SA4) at 100 kfps both for understanding as sample crushing proceeds and for DIC analysis. The system set up is reported in Figure 5b. In the enlarged image it is possible to observe the sample mounted on the apparatus.

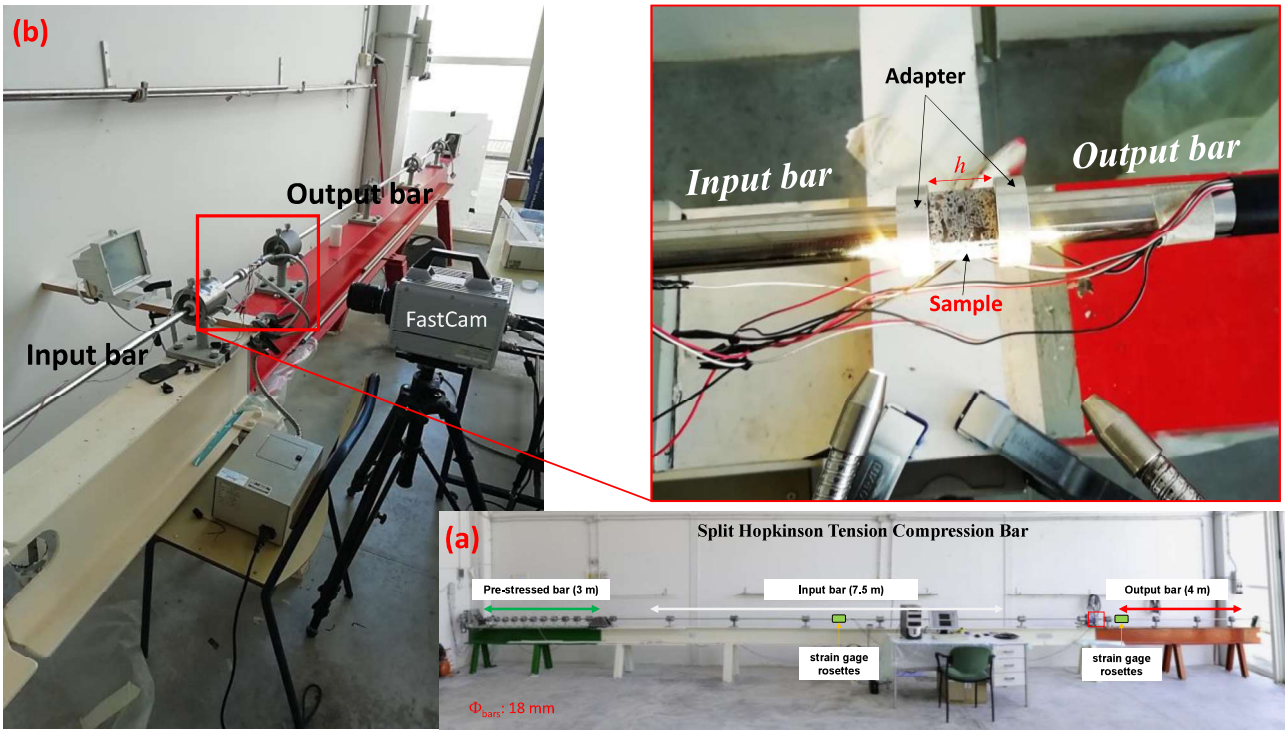

Figure 5. SHBar set up; sample mounted on the apparatus before the test

2.4 MESOSCOPIC 3D SAMPLE GENERATION

3D model of the samples, obtained with different values and distributions of porosity, is useful to understand the effects of metallic foam porosity on stress-strain localization during collapse, as demonstrated in [29]. In this paper, mesoscopic geometrical models with stochastic cell distributions have been built to confirm the experimented behaviour and its material model calibration, in accordance with the morphological data measured on the foam ingot.

The modelling approach is based on a surface tessellation of cells that are derived from a Voronoi diagram [33]. The Voronoi diagram represents a network of surfaces that describes the 3D porosity envelops as geometrical-simply-connected volumes. It is derived from a set of randomly-placed 3D points (called seeds), inseminated inside a control volume, V. The number of seeds is defined so that an associated uniform first-attempt cell radius may reproduce the actual density of the foam, despite possible overlapping. Figure 6a shows an example in case of 2D cells, Figure 6b represents the 2D Voronoi diagram associated to the seeds in a control surface of 40x40 mm.

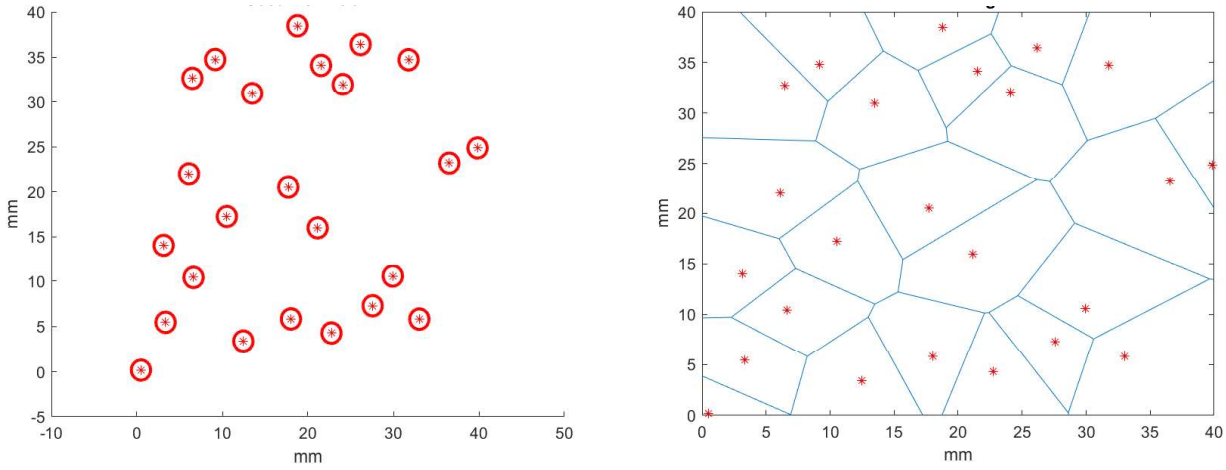

(a) (b)

Figure 6. 2D example of cell generation: (a) seed definition; (b) associated Voronoi diagram

The foam model is obtained after that all the cells of the Voronoi diagram have been "inward" scaled so that effective density is finally achieved (Figure 7a).

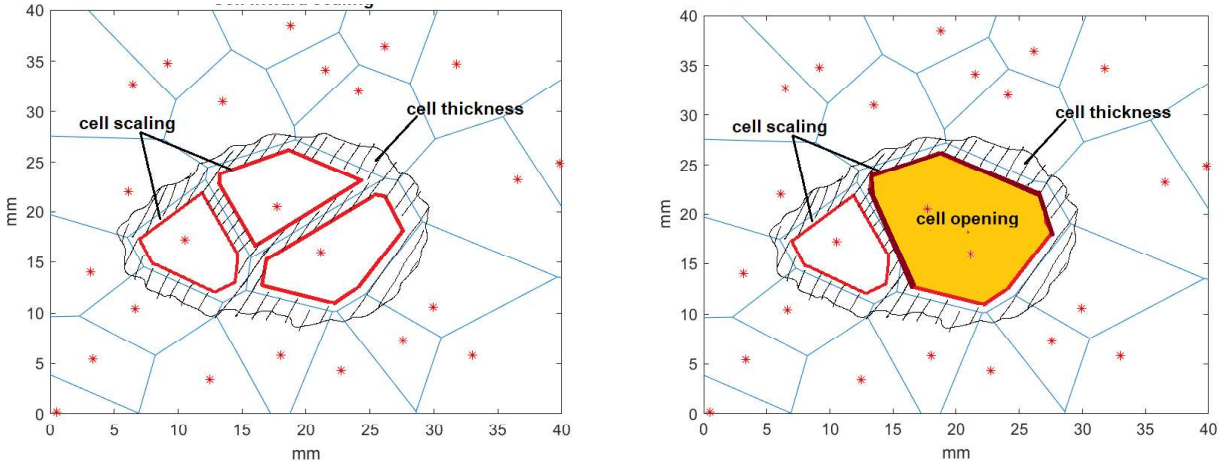

(a) (b)

Figure 7. 2D example of cell generation: (a) cell inward scaling; (b) cell opening to build outlier cavities

By this procedure, cells are naturally tessellated in triangles, but their mesh size is not optimized for FEA simulation and their approximated roundness may not satisfy the actual roundness distribution of the foam. According to this, mesh density is refined for achieving optimal FEA conditions (usually minimum element length ≥0.8 mm). Mesh refinement does not change mesh vertex positions thus it does not affect cell sphericity. For this reason, average cell sphericity is checked to verify that it is in a range compatible with the roundness experimental data coming from the image analysis. If it is not verified an iterative tuning may be done through mesh smoothing [34].

The result of this process is a cell boundary mesh made of triangles (FEA element type: shell). The 3D model is obtained through tetramesh, anchored to the cell boundary shell mesh and to a regular shell mesh of the faces that represent the outer surface of the control volume, V, in which the seeds were

generated. Applying this workflow in Hyperworks © final tetramesh will be able to pass all the quality checks, without relevant problems.

To highlight the local stress-strain effects induced by larger macrocavities, aggregation of cells may be inserted opening the Voronoi diagram network before the cell inward scaling (Figure 7b). It can be done through an interactive definition of the equivalent square volume of the aggregation (defined by the square centre position and its diagonal), in which a large cell outlier can be generated by removing the cell walls inside it and then, after cell inward scaling, reshaping the resulting void through the previously- applied mesh density and smoothing values.

3 RESULTS AND DISCUSSION

3.1 EXPERIMENTAL TESTING

Tests in quasi-static conditions have been carried out both to analyse the foam behaviour and to verify that the results were in agreement with the quasi-static behaviour under compression investigated in the past by some of the authors [35][36]. The test results are in accordance with the typical stress-strain curve of aluminium alloy foam in the same loading conditions and confirm the foam excellent efficiency [37]. The compression behaviour of the studied foam is characterized by an initial peak after the elastic region, and by a jagged behaviour in correspondence of the plateau region due to the fact that the cell walls under compression do not bend, but they fracture in a brittle way during compaction. Figure 8 shows the experimental engineering stress-strain curve highlighting the collapse initiation strain, ε_{c0}, that unambiguously has been identified as the strain corresponding to σ_{c0}, which is the start of the plateau stage, and the onset of densification strain ε_{d0}, determined as the maximum of the energy absorption efficiency. The onset of densification strain was evaluated as proposed by Li et al [38] and later widely accepted and increasingly used by researchers for various types of cellular materials [37][39][40][41]. In detail, the energy absorption efficiency e [42][43] was calculate as defined by

$$e(\varepsilon) = \frac{\int \sigma(\varepsilon) \cdot d\varepsilon}{\sigma(\varepsilon)} \quad (7)$$

where σ and ε are the nominal compressive stress and strain, respectively.

The densification stage begins (or the plateau stage ends) when e reaches a global maximum in the efficiency-strain curve:

$$\left.\frac{de(\varepsilon)}{d\varepsilon}\right|_{\varepsilon=\varepsilon_{d0}} = 0 \qquad (8)$$

where ε_{d0} is the densification initiation strain. The collapse initiation stress, σ_{c0}, is usually used to indicate the yield strength, which can be obtained as the first peak stress or the stress at which the tangent modulus is the first minimum. The initial yield strength of a cellular material can also be determined as in [7] by an offset yield stress (e.g., 0.3% offset axial strain). However, it requires the knowledge of the elastic modulus whose accurate measurement needs a not negligible effort because it may vary with strain [40][44].

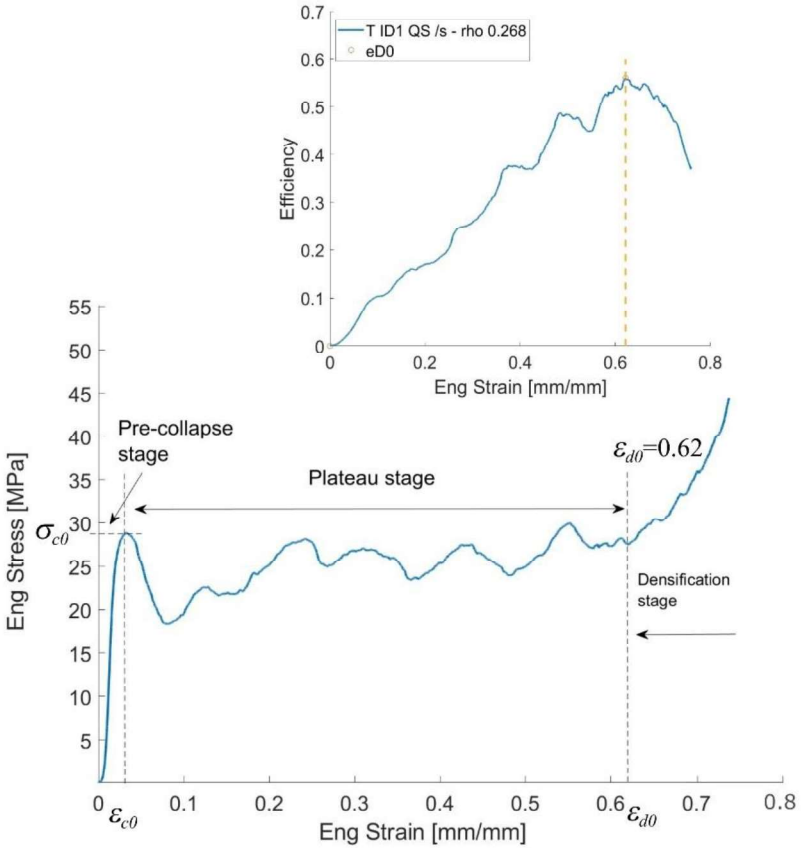

Figure 8. Diagram of the experimental QS engineering stress-strain curve illustrating the three compression stages; in the insert the calculated efficiency

Engineering stress (force/original cross sectional area) and strain (displacement/original length of the foam specimen) were calculated for dynamic tests using the formulas and procedure described in section 2.3.2. The obtained engineering stress-strain curves, for different strain rates, are shown in Figure 9. For all the tests the strain rate was almost constant (Figure 9c).

Dynamic tests confirm the excellent efficiency shown from the quasi-static (QS) ones. Indeed, the curves are characterized by a stiff region with a local peak stress (pre-collapse stage) followed by a plateau. However, the shorter loading pulse related to dynamic compression tests made by SHB did

not allow to reach the densification stage. Nevertheless, also the numerical simulations results that are reported in the next sections, agree with the experimental ones, showing a local peak stress followed by a plateau.

In Figure 10 the quasi-static and dynamic tests are reported together. The results of the tests previously made by some of the authors in [36] are considered too.

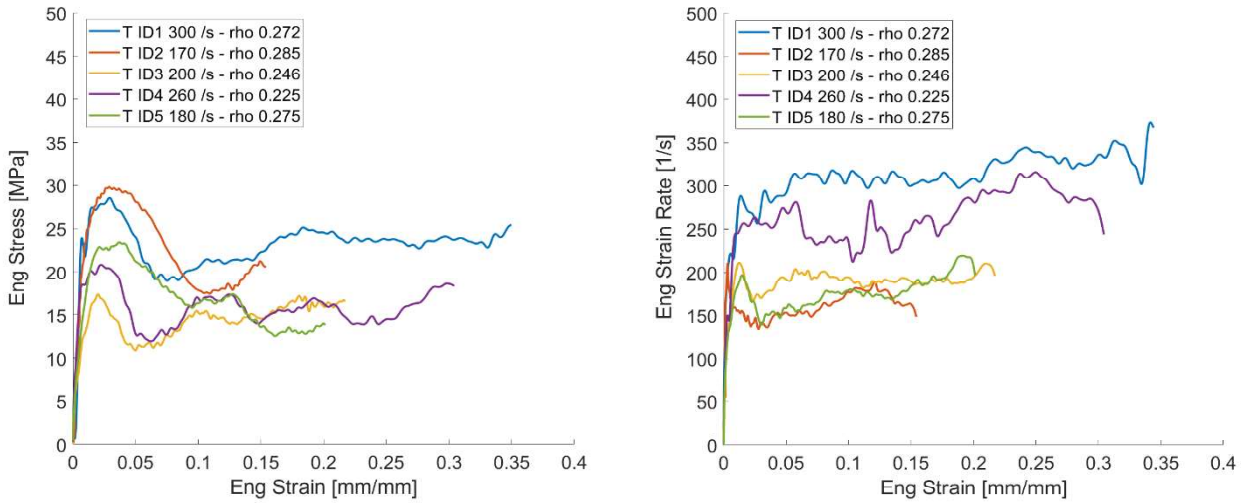

Figure 9. (a) Dynamic engineering stress-strain curves and (b) strain rate-strain curve

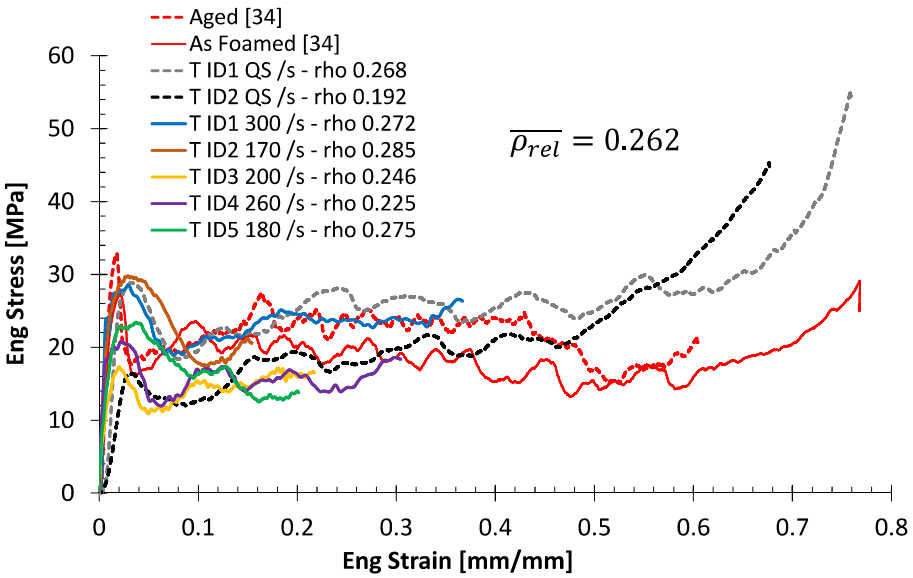

Figure 10. Experimental engineering stress-strain curve

Furthermore, despite the effort to reduce the size effect (the specimen size was chosen as large as possible respecting what is established in literature) the curves highlight a strong dispersion. This dispersion makes the analysis of the mechanical properties of the foam difficult; moreover, no general

trend with strain rate can be found, as cell size and morphology distributions play a predominant role. Hence, a mesoscale FEA model should be implemented, capable of reproducing the cells according to the real statistical distribution derived from the morphological and topological analyses.

3.1.1 Deformation pattern

All dynamic tests have been recorded by a FastCam in order to analyse the deformation during crushing. Figure 11 shows the photographs captured in different moments of the dynamic tests, the DIC analysis made to control the pattern deformation and the loads on both sample sides. For all cases, deformation starts in the weakest bands when the sample is crushed. These bands are shown in Figure 11b by a white central line with two white lines showing the boundaries. They are randomly distributed in the specimen as it begins to crush: sometimes they are close to an edge, sometimes they are in the central area and sometimes there are more than one. In Figure 11d the loads acting on the left and right side of the sample during the test are also reported. Apart from some oscillations, which are normal on the input bar side in dynamic SHB tests, the major part of the test occurred in dynamic equilibrium.

As the crushing proceeds, further deformation occurs in other regions with other cells that collapse simultaneously. It must be stressed that the foam deformation is not characterised by the simple cell collapse but principally by the fracture of cell walls (see the attached video: “Test_ID1_Movie.avi”).

Figure 12 shows the first and one of the last acquired images, for each dynamic test; the last DIC converged step is reported too.

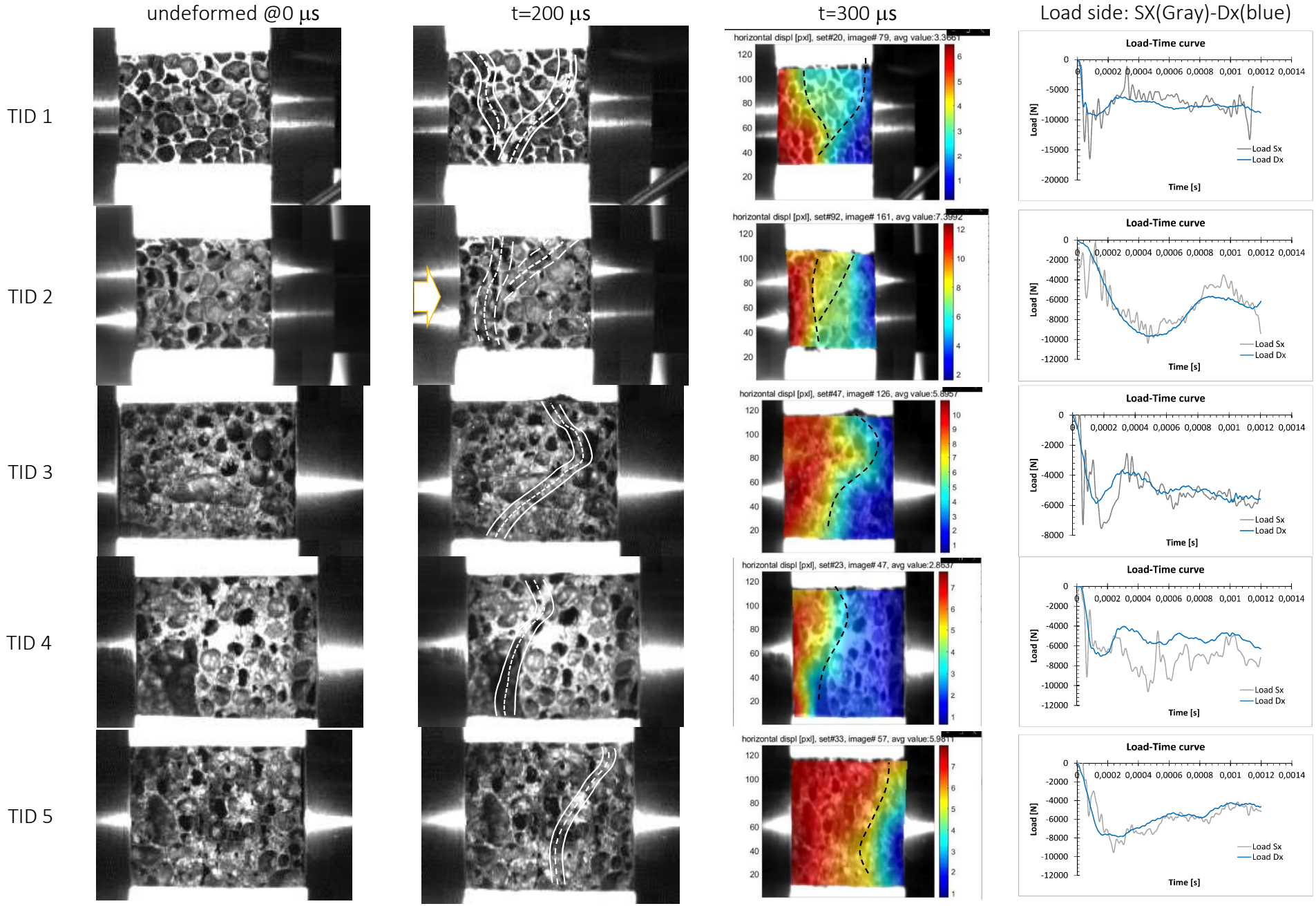

Figure 11. Dynamic compression process images with highlighted crash bands;(a)-(b) sample images at two different instants of time, (c) DIC displacement, (d) load on sample ends

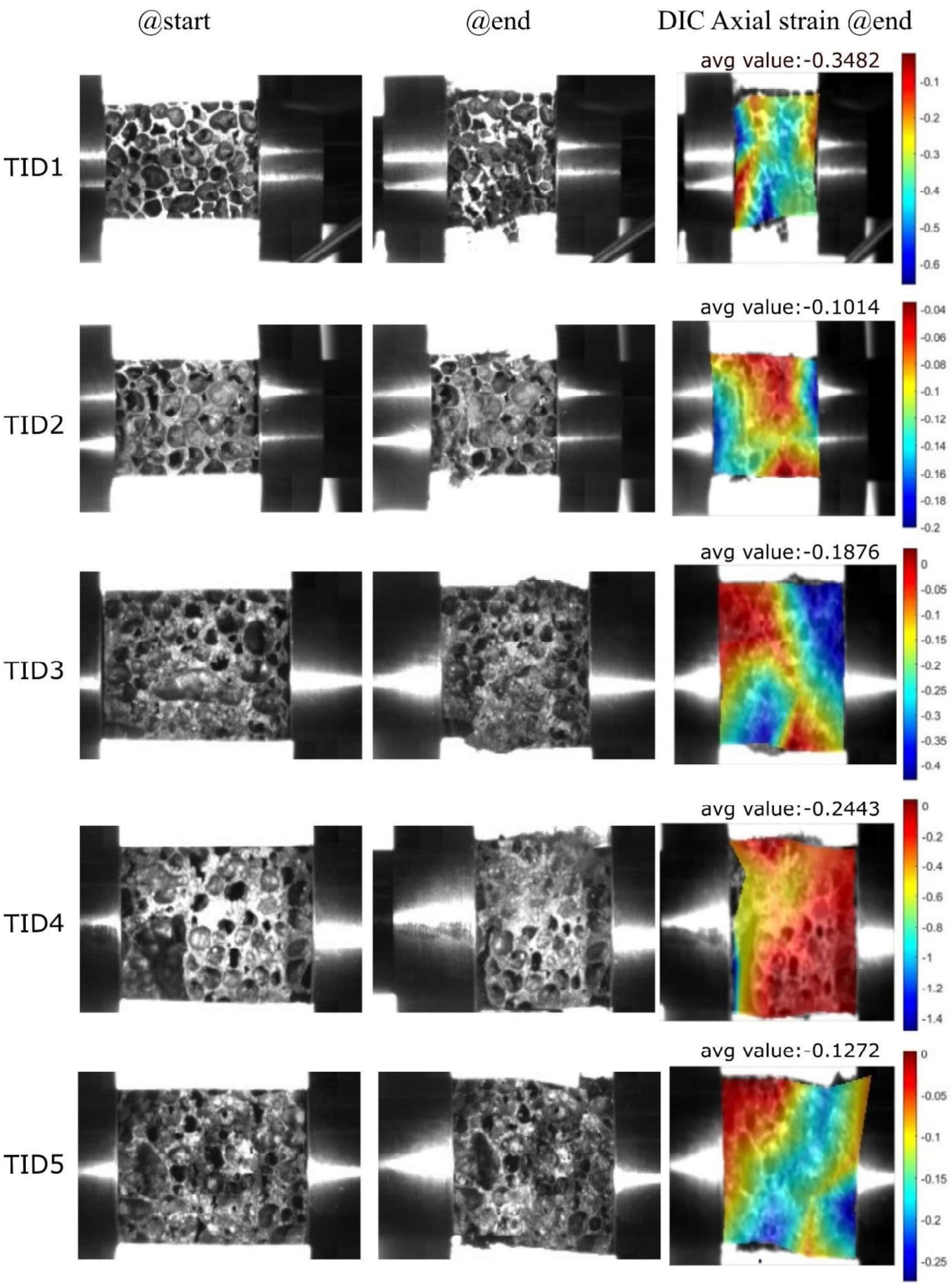

Figure 12. Dynamic compression process images at the start and the end of test; the DIC axial strain at the end of test

3.1.2 Fracture surface analysis

Fracture surfaces of broken specimens after dynamic tests have been analysed in order to study the fracture mechanisms and to confirm the deformation pattern highlighted in the previous section.

Figure 13 shows the fracture surface morphology. This figure highlights that the fracture mode is predominantly brittle although in some areas a mixed mode fracture can be observed. Figure 13a shows the morphology of the fracture propagating through a shrinkage cavity, which is visible at the front in the micrograph: dendrites can be clearly observed. The tips of dendrite branches are indicated by arrows. In Figure 13b the transgranular fracture coexists with very small areas characterised by tiny dimples (dashed circle). These observations confirm that the studied aluminium foams have a predominant brittle behaviour that justifies the results observed during the mechanical tests, confirming that, during deformation, cell walls break instead of bending.

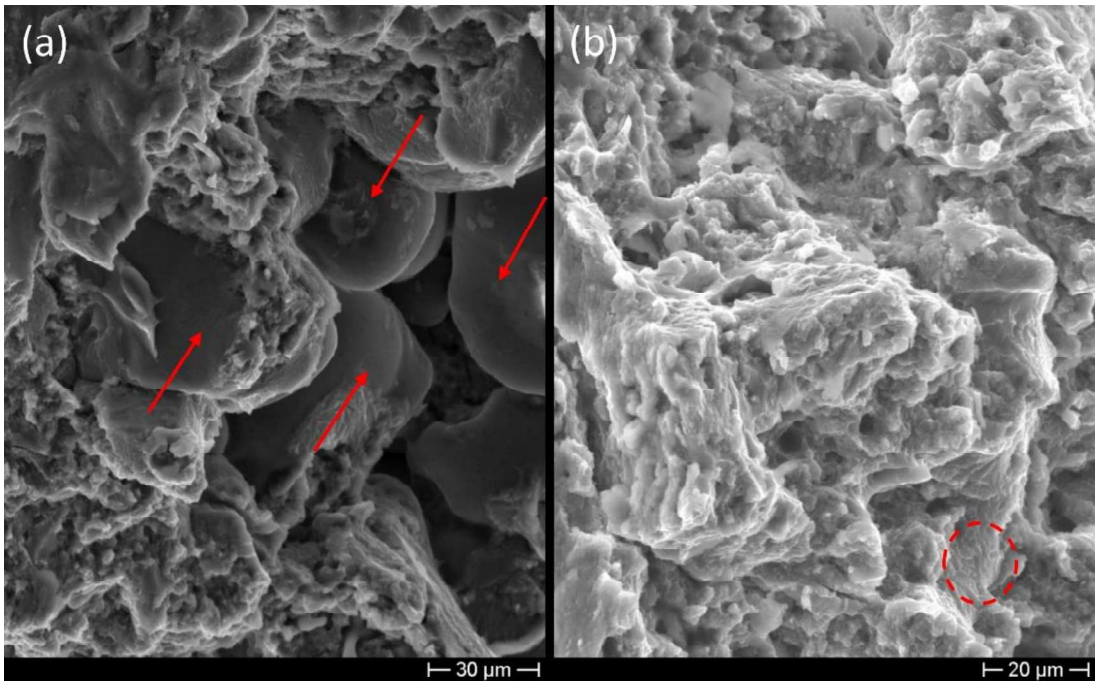

Figure 13. SEM micrographs showing the fracture surfaces of specimens broken during the dynamic mechanical tests. Figure 13a shows at the front dendrite branches coming out of the shrinkage cavity, Figure 13b shows the fracture surface.

3.2 MORPHOLOGICAL AND TOPOLOGICAL ANALYSIS RESULTS

The results of the morphological and topological analyses are shown by the bar charts of the probability densities given in Figure 14. Each category along the x-axis represents an interval of cell area and roundness; moreover, the categories along the x-axis have 4 bars which indicate the result

for each slice shown in Figure 1. The occurrence frequency of each interval category is reported on the y-axis.

In Figure 14a it is evident that approximately 80% of the cells have an area around 2 mm^2, slightly less than 10% are around 4 mm^2, and the remainder is spread over larger areas. It is also noted that the smaller cells are in slices 1 and 2. By observing the roundness distribution in Figure 14b, it is noted that approximately 80% of the cells are characterized by a roundness in the range 1.0-1.9. Figure 14 shows also that on all the examined sections there could be elongated (characterized by high R) and big cells (characterized by large area) that can affect the foam mechanical behaviour. This is possibly due to specific condition of the foaming process and to the fact that cells could be oriented in a direction that depends on the position of the mould.

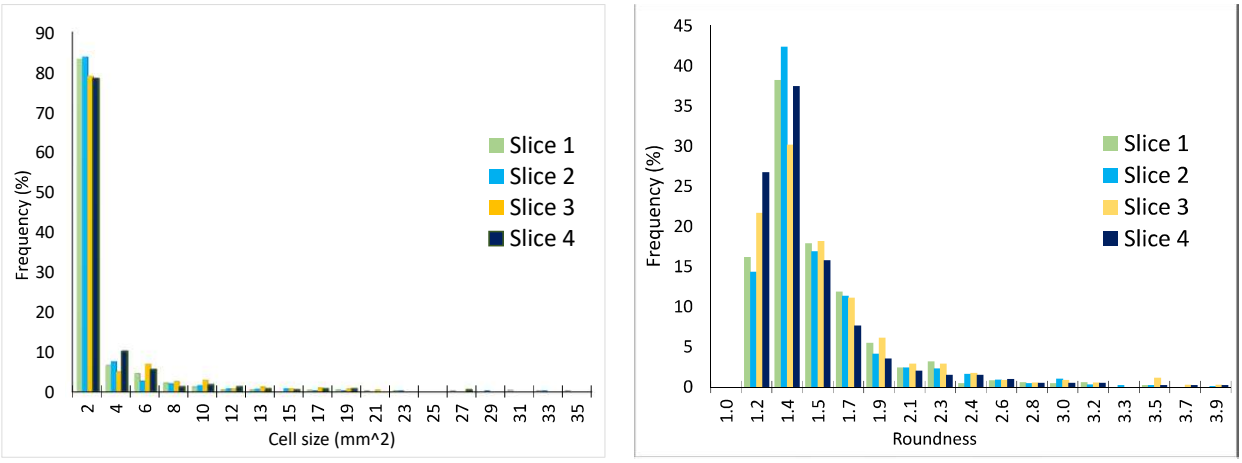

(a) (b)

Figure 14. Cell area and cell roundness distribution in different slices of the specimen.

By analysing the distributions of cell area and roundness it can be pointed out how they follow well an Exponential and Weibull distribution, respectively (Figure 15). As far as the cell area is concerned, cell having a diameter up to 2 have been considered porosities related to a microscale level, and then they are not included in the fitting. With regard to the roundness distribution, remembering that R values less than 1 do not exist, the data reported in Figure 15a have been shifted by 1 before the statistical analysis. The goodness of the fitting is confirmed by both the fit of the cumulative probability function and probability plot of the data.

By further analysing the distributions of cell area and roundness, it was noted that they could be fitted by a negative Exponential distribution and by a Weibull distribution, respectively (Figure 15).

The probability density functions are represented by

$$pdf(A_{cell}) = \frac{1}{\mu} e^{\frac{-A_{cell}}{\mu}} \quad (9)$$

$$pdf(R) = \left(\frac{\alpha}{R_0^{\alpha}} R^{\alpha-1} \cdot e^{\left[-\left(\frac{R}{R_0}\right)^{\alpha}\right]} \right) \quad (10)$$

where, as well known, μ is the average cell area, R_0 and α are the scale and shape parameters of the Weibull distribution of the cell Roundness; note that equation (10) represent the Weibull function with location parameter set 1.0, which is the minimum admissible value of R (the data reported in Figure 15a have been shifted by 1 before the statistical analysis). As far as the cell area is concerned, cells having an area up to 2 mm^2 (first category in the bar plot of Figure 14a) have been considered porosities related to a microscale level, and then they are not included in the analysis (they possibly have limited effect on the global stress-strain behaviour and, moreover, they are very difficult to be produced into the following mesoscale model).

Hence, a fitting of the negative Exponential and Weibull laws has been performed, excluding the cells with area lower than 2 mm^2; a good matching between the experimental and analytical statistical data can be observed in Figure 15, in terms of both probability density and cumulative distribution. Table 3 reports the best fit coefficients of the negative Exponential and Weibull distributions; these coefficients will be used in the volume mesh generation for the mesoscopic numerical analysis (section 3.3) and in the unified material model definition (section 3.4).

Table 3. Statistical distribution coefficients

Cell area [mm^2]	*Cell Roundness*	
μ	α	R_0
5.30	1.55	0.60

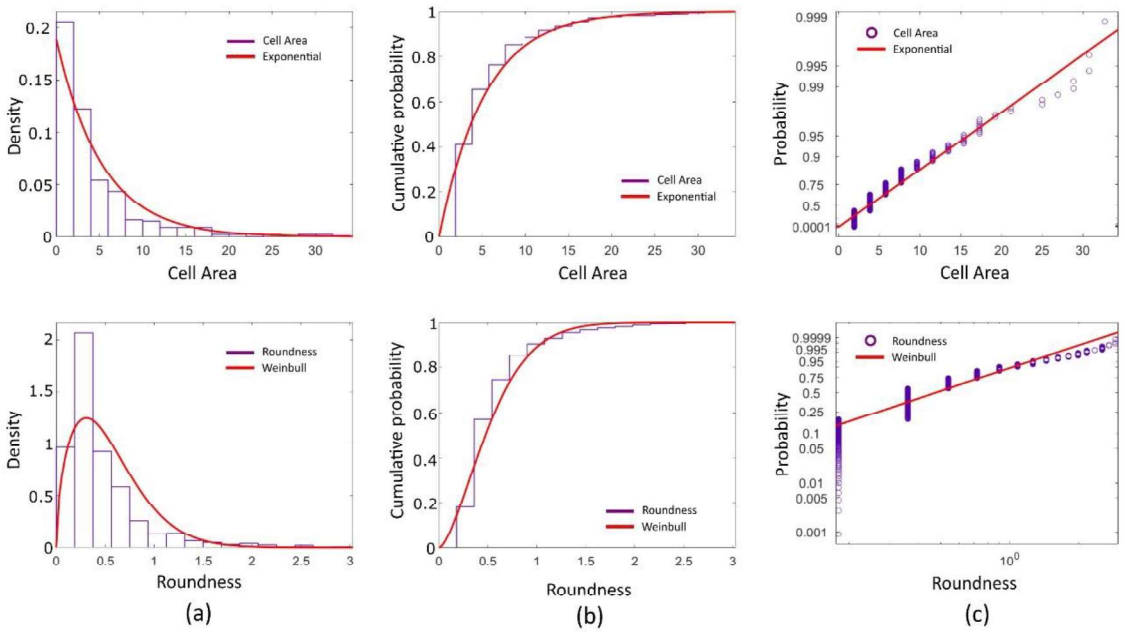

Figure 15.Cell area and cell roundness distribution fitting (a), Computed cumulative probability function (b) and Probability plot of the data (c)

3.3 NUMERICAL SIMULATION RESULTS

The mesoscopic FEA model has been generated as described in section 2.4 considering the morphological and topological analysis results reported in the section 3.2.

Figure 16a provides a view of the generated 3D model. It is a square volume of 50x50x50 mm with 1978 seeds that are associated with a uniform first-attempt radius of about 1.64 mm and inserted in a control volume of 40x40x40 mm. It is worth pointing out that the distribution of the seeds, in this case, has been included in a control volume smaller than the overall 3D model, to avoid material localization at the boundary of the specimens. In fact, doing so a more uniform wall thickness may be achieved by cutting the external skin.

Figure 16b shows the comparison between the mesoscale morphology with and without cell opening (respectively in yellow and cyan), referred to the central section where opening is inserted. The cell opening has been positioned on the bottom part of the control volume. It has been achieved by imposing an equivalent volume of aggregation of 30 mm^2, to fit the largest outlier radius found in the experimental distribution (Figure 14). No smoothing has been applied since the average sphericity check has been positively passed.

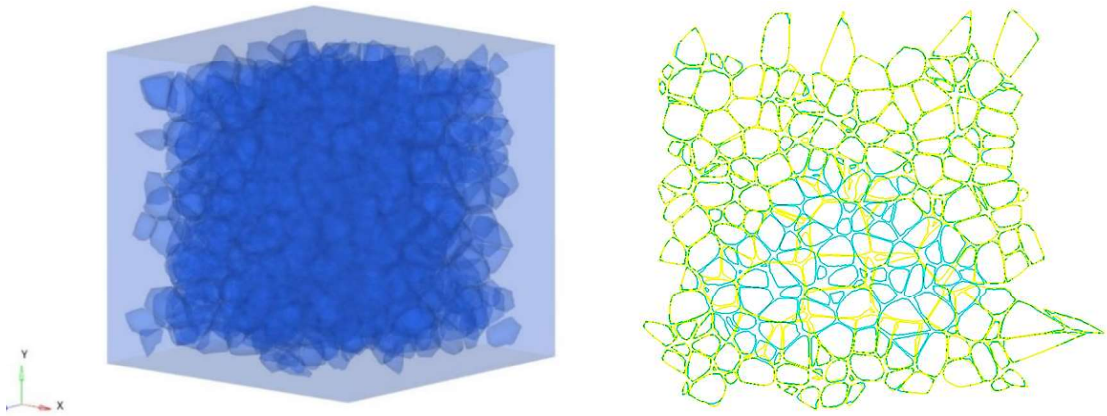

(a) (b)

Figure 16. (a) 3D mesoscale model with external skin (50x50x50 mm), (b) cell morphology, in yellow the model with cell opening, in cyan the reference model

Concerning the FEA mesh characteristics, the minimum element size is 0.8 mm. This value affects the minimum cell radius that can be achieved. In particular, porosity with radius less than minimum element size must be considered as a porosity related to a microscale level, thus not included during the seed generation. This determines that, in the FEA mesoscale model, the minimum achievable cell area is about 4 mm^2 (that corresponds to the second most populated bin of cell size distribution shown in Figure 14).

Samples coming from volume mesh with and without a larger cavity provided to simulate a localized outlier cell have been extracted as shown in Figure 17.

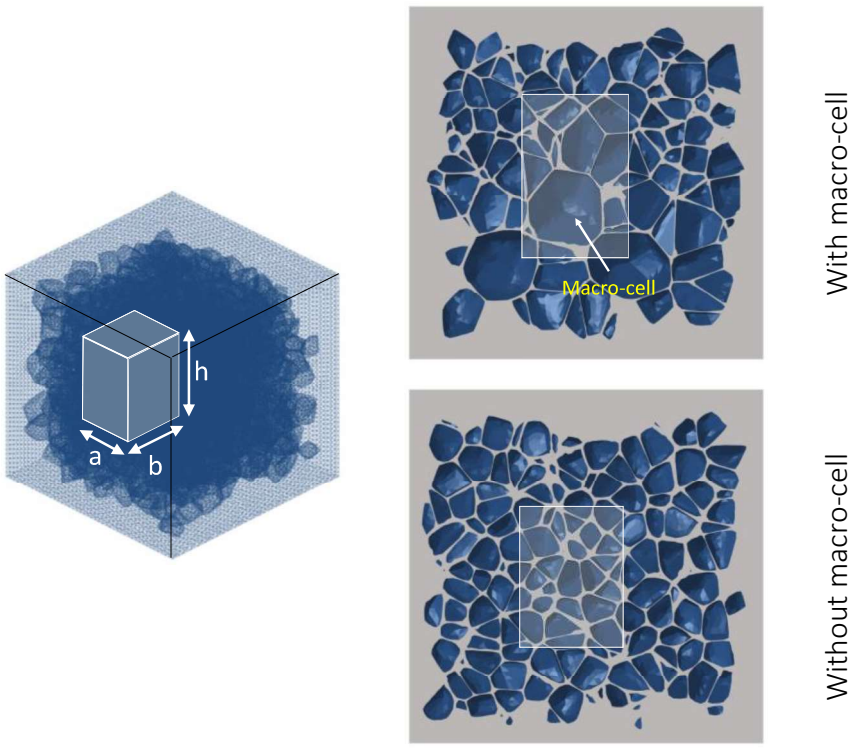

Figure 17. (a) Discretazed ingot with the extracted sample position and (b) their position in sections.

Figure 18a shows the sections where macroscopic differences among the cells are visible. Other cavities in the sections have been maintained almost equal. Simulations have been done through the Hyperworks suite. Material law has been modelled as a Johnson-Cook viscoplastic law according to [45][46], taking into account micro-hardness results. Auto-contact and failure criteria have been implemented too.

In Figure 18b the equivalent plastic strain distribution at the end of simulations is reported. It can be seen the cell crushing concentrates in correspondence of the macro-cells wall and proceeds near them, instead, in the absence of macro-cell the deformation starts in correspondence of the weakest bands. These bands are delimited in the figure by two continuous white lines with a white central dashed line.

Figure 19 shows the comparison between the stress-strain engineering curves, obtained by means of the numerical simulation, and the experimental ones. The simulation confirms the effect of cell dimensions on the first prominent peak of stress σ_{c0} and the optimum behaviour of this type of foam as core for energy absorber devices, highlighted by the subsequent stress plateau. The absence of densification in numerical simulation is due to convergence problems. The major prominence of the initial peak of stress found in the numerical simulations may be correlated to the absence of small porosities with area less than 4 mm^2, as previously described.

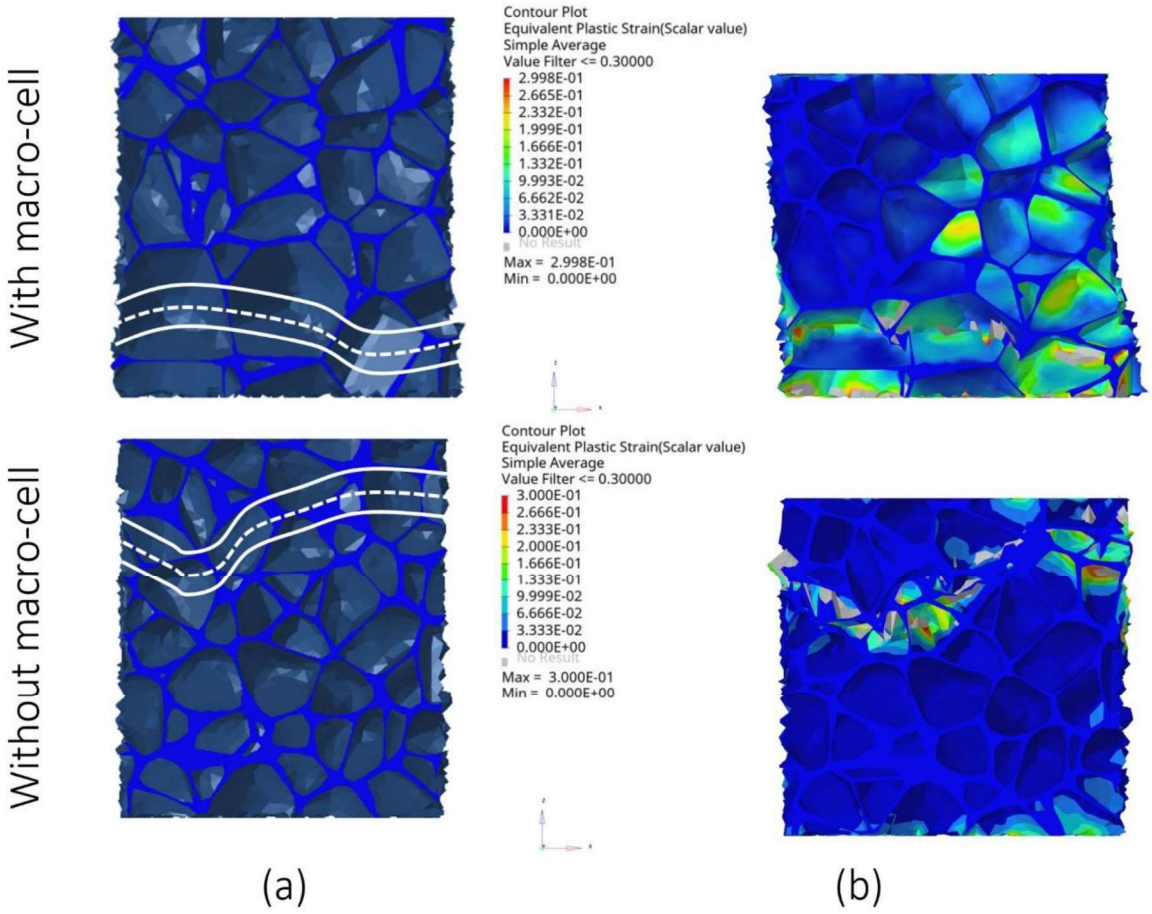

Figure 18. Results (a) start and (b) end of the numerical simulation.

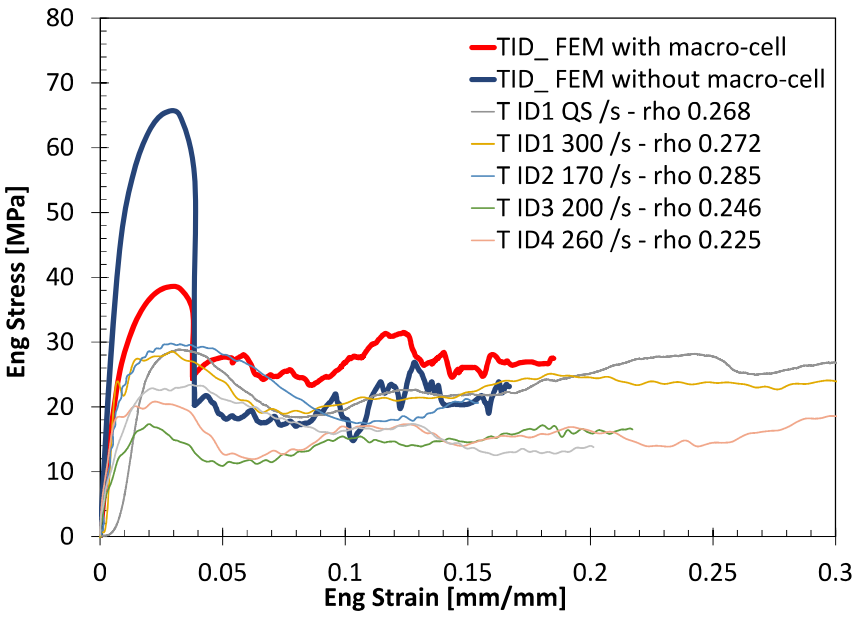

Figure 19. Experimental and numerical engineering stress-strain curves

3.4 MODEL DEFINITION AND CALIBRATION ON AA7075-T6 FOAM

Different models are available in the literature to describe the cellular solid behaviour. In the present paper the five-parameter Avalle [47] model has been considered, which is given by

$$\sigma = A\left(1 - e^{(-E/A)\varepsilon(1-\varepsilon)^m}\right) + B\left(\frac{\varepsilon}{1-\varepsilon}\right)^n \quad (11)$$

where σ and ε are engineering stress and strain, respectively, considered positive in compression. In (11), E represents the elastic modulus, m is a coefficient governing the transition from the linear elastic region to the plateau region, A is the plateau stress; B and n coefficients describe the densification region. The parameters *E, A* and *B* are density dependent, while parameters *m* and *n* are not. Although this model represents the loading characteristics of foams reasonably well, it does not consider neither the first collapse initiation stress nor the strain rate effect.

In order to describe the shape of the stress-strain curves from the collapse initiation stress (σ_{c0}) to the plateau stress (σ_p), the first term of Nowak and Peçherski [48] model (equation (12)) has been used.

$$\overline{NK} = \left(1 - \frac{f_{SB_0}}{1 + e^{a-b\varepsilon}}\right) \quad (12)$$

While this term represents a sort of shape factor, the entity of the stress drop from the collapse stress σ_{c0} to the plateau stress σ_p is determined by the morphology and topology of the cells. On first approximation, it is accepted a constant drop between initial stress and plateau (Figure 20a) so f_{SB_0}, a, b can be immediately found (Table 4).

Table 4. Novak term coefficients

f_{sB0}	a	b
0.25	6	110

It has been assumed that the plateau stress is governed by the average roundness $\bar{R}$ and by the largest cell area $A_{\text{cell,max}}$ of the given sample of material, according to a negative power law as in equation (14). In addition, even if the strain rate sensitivity of the base material has a limited effect if compared to the dispersion due to cells inhomogeneity, it has been accounted for by the classical Johnson-Cook term of the kind

$$C(\dot{\varepsilon}) = 1 + c \cdot \ln\left(\frac{\dot{\varepsilon}}{\dot{\varepsilon}_0}\right) \quad (13)$$

The coefficients c and $\dot{\varepsilon}_0$, representing the strain rate sensitivity coefficient and the threshold of strain rate, respectively, have been borrowed by the literature [26], and are reported for the sake of completeness in Table 5. If they are not available in literature, they can be obtained calibrating the Johnson-Cook model on experimental tests carried out on the base material at high strain rate.

Table 5. Johnson-Cook term coefficients for strain sensitivity of base material [26]

c	$\dot{\varepsilon}_0$ [1/s]
0.058	144

Then, the expression of the plateau stress becomes:

$$\sigma_p = \sigma_{c0} \cdot C(\dot{\varepsilon}) \cdot \left(\bar{R} \cdot A_{cell,max}\right)^{-q} \quad (14)$$

where q is a positive non-dimensional parameter to be calibrated. The final expression of the adopted constitutive model is:

$$\sigma_{mod} = \overline{NK} \cdot \sigma_p \cdot \left(1 - e^{\left(-E/\sigma_p\right)\varepsilon(1-\varepsilon)^m}\right) + B\left(\frac{\varepsilon}{1-\varepsilon}\right)^n \quad (15)$$

where σ_p given by (14) is used in place of A of equation (11).

The experimental curves previously shown in Figure 10 have been used to obtain the best fit coefficients of the proposed model.

It is noteworthy that the Young modulus E has been evaluated separately using only the stress data before the collapse initiation stress, and its values was found to be 3500 MPa. Moreover, since the transition from elastic region to the plateau region is described by $\overline{NK}$ (12), the m term was held constant and set to 1.0; in the case of foams that do not exhibit a collapse initiation stress, the $\overline{NK}$ should be set to 1 and m should be calibrated.

Hence, the fitting procedure aimed at finding the best values of 4 coefficients that minimize the difference between the experimental data and the analytical ones computed with equation (15). The 4 coefficients are, the collapse initiation stress σ_{c0}, the power law exponent q that reduces the plateau stress accounting for cells statistical distribution, B and n that describe the densification region.

The coefficients of best fit are reported in Table 6

Table 6. Fitting coefficients of the equivalent material model

σ_{c0} [MPa]	q	B [MPa]	n
52	0.36	0.48	3.6

All the coefficients have a reasonable value if their physical meaning is considered: the coefficient σ_{c0} is the highest possible peak stress for the given relative density, which is achieved in the ideal case of cells with largest cell area of 2 mm^2 and average roundness of 1.0. The values of *B* and *n* are of the same order of the values that can be found in the literature where the same model [49] was used; actually, the term *n* is sometimes referred to as a sort of polytropic exponent accounting for gas compression and, especially for polymeric closed cell foams, its value should be around 1.4 [50]; however it is reasonable that the value is higher here, since it is intended to model the steep strength increase due to material compaction.

As far as f_{sB0}, a and b are considered, they are non-dimensional parameters that describe analytically the stress drop from the peak stress, and have been firstly adopted by [48] to represent the strength collapse in materials exhibiting shear bands. Although they do not have an explicit physical meaning, the values reported in Table 4 are reasonable; the value of *a* is similar to that found in [48]. As far as f_{sB0} and *b* are concerned, the difference is related to how suddenly the stress drops as a function of strain. Moreover, it can be argued that, even if the real behaviour of the material at a microscopic level could be different, the crash bands shown in Figure 11 have a similar effect on the global strength curve compared to the shear band phenomenon.

Finally, *q* is a positive number, meaning that the strength reduces as the largest cell area and/or average cell roundness increases, and depends on the cell statistical distribution.

It is noteworthy that the strain rate effect, in the range investigated, seems to be secondary and negligible in comparison with the effect of cell morphology and of the brittle behaviour of the material.

The results of the model fitting are shown in in Figure 20, where the experimental stress vs strain curves are compared to the analytical ones obtained using equation (15) with the best fit coefficients given in Table 6.

The different contributions of each term are highlighted in Figure 20a: the blue and orange lines represent the stress due to the first and second term of the new model, respectively; the green line represents the multiplicative Nowak term $\overline{NK}$ given by equation (14); the dashed red line shows the overall response of the model. The calibration results for the extreme values of cells area and

roundness considered in the morphological and topological analysis are shown in Figure 20b: the thick red curve refer to the combination $A_{cell,max}$ = 4 mm^2 and R=1.2, while the thick orange curve refer to the combination $A_{cell,max}$ = 30 mm^2 and R = 1.9; these two curves span all the experimental curves, and represent a sort of upper and lower boundary of the expected material strength, if random values of cell area and roundness are extracted from the negative Exponential and Weibull distributions.

Finally, the efficiency (e) of energy absorption has be computed, according to equation (7), and compared to the experimental one (Figure 20c). A good matching is also observed for efficiency.

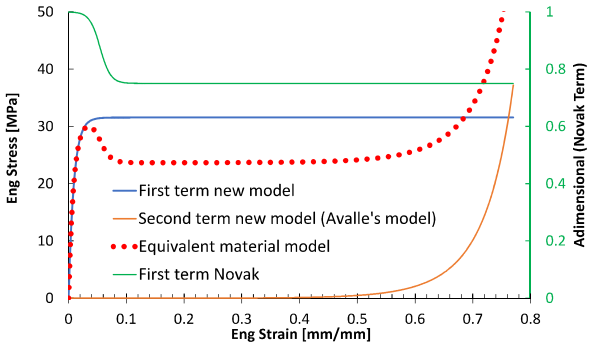

(a)

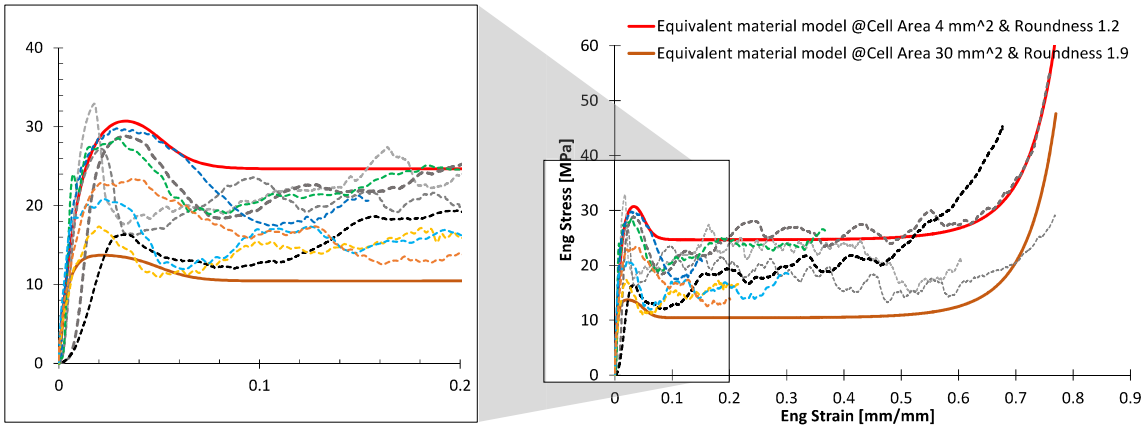

(b)

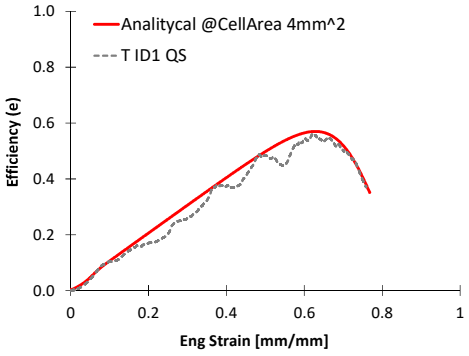

(c)

Figure 20. Comparison between analytical and experimental curves; (a) different contributions of each term of the model, (b) material model @ extreme cell area and roundness, (c) energy efficiency absorption

4 CONCLUSIONS

This paper focuses on a methodology, supported by numerical mesoscopic models, to define a systematic procedure to overcome the uncertainty in the identification of the RVE suitable for the experimental tests. Moreover, setting up this procedure could improve the understanding of the experimental (quasi-static and dynamic test), analytical (material model chosen) and numerical (cellular structures simulations) observations. The proposed procedure considers the role of geometric cell discontinuities in the mechanical characterization of a cellular material as well as the fracture behaviour and the strain rate sensitivity of the base material. A closed cells AA7075-T6 aluminium foam having an average relative density of $\overline{\rho_{rel}} = 0.262$ and produced by means of powder technology have been analysed.

The obtained results can be summarized as follows:

- the foam inhomogeneity leads to a scattering of results both in terms of stress–strain curves and maximum strength. The scatter not always is related to wrong RVE identification.
- morphology, topology and anomalies (i.e. large anomalous cell) of cell structure together with the brittle behaviour of base material can make negligible or not directly evaluable the effect of strain rate on the cellular material properties. Hence, foams with high inhomogeneity, characterized by macroscopic and microscopic discontinuities, lead to an uncertain evaluation of foam properties by the simple analysis of the stress-strain curves, making necessary a mesoscale modelling.
- the mesoscopic FEA volume mesh model has been generated considering the morphological and topological analysis results. The mesoscopic model confirms the effect of cell dimension and roundness on the first prominent peak of stress σ_{c0} and the good behaviour of this type of foam as core for energy absorber devices. This good behaviour is justified by the subsequent stress plateau.
- although morphological analysis highlighted 80% of microscopic porosities in the cell wall thickness, the mesoscopic FEA proved, in accordance to experimental images, that the start of the specimen collapse is along bands associated to the few largest mesoscopic cells.
- the strain rate effect, in the investigated range (10^{-3} to $\sim 3x10^{2}s^{-1}$), is secondary and almost negligible if compared to the effect of cell morphology and to the effect of the brittle behaviour of the bulk material. However, the fracture brittle behaviour of cells walls, observed experimentally, supports and makes the studied alloy foam more suitable for the production of energy absorption devices. The high strength of the base material, coupled with its brittle behaviour, improves the foam energy absorption efficiency.

- the equivalent material model, based on the five-parameters Avalle model, has been implemented, calibrated and analytically verified. The model parameters were identified with the dispersion by performing the morphological and topological analyses. Moreover, the strain rate sensitivity of base material and its mode of failure have been also taken into account. Further validations will be carried out on foams with different morphologies and base materials characteristics, to assess the final capability of the model.

5 DATA AVAILABILITY

The raw data required to reproduce these findings cannot be shared at this time due to technical or time limitations. The processed data required to reproduce these findings are available to download from

[https://univaq-my.sharepoint.com/:f:/g/personal/edoardo_mancini_univaq_it/Eguty_oLYR9OvJ-XIsDA7GABUMgMuGpHZvqSeXg75wpufQ?e=txbIvl].

6 REFERENCES

[1] J.L. Gibson, F.M. Ashby, Celluar solids: structure and properties, 2 ed. Cambridge University Press, 1997.

[2] Elliott J. C., Method of Producing metal foam, U.S. Patent No 2,751, 289, 1956.

[3] J. Banhart, Manufacture, characterisation and application of cellular metals and metal foams, Prog. Mater. Sci. 46 (2001) 559–632. https://doi.org/10.1016/S0079-6425(00)00002-5.

[4] P. Patel, P.P. Bhingole, D. Makwana, Manufacturing, characterization and applications of lightweight metallic foams for structural applications: Review, Mater. Today Proc. 5 (2018) 20391–20402. https://doi.org/10.1016/j.matpr.2018.06.414.

[5] L.J.G. M.F. Ashby, A.G. Evans, N.A. Fleck, J.W.H. and H.N.G. Wadley, Metal Foams : A Design Guide, Oxford: Butterworth-Heinemann, 2000.

[6] Y. Sun, Q.M. Li, Dynamic compressive behaviour of cellular materials: A review of phenomenon, mechanism and modelling, Int. J. Impact Eng. 112 (2018) 74–115. https://doi.org/10.1016/j.ijimpeng.2017.10.006.

[7] V.S. Deshpande, N.A. Fleck, Isotropic constitutive models for metallic foams, J. Mech. Phys. Solids. 48 (2000) 1253–1283. https://doi.org/10.1016/S0022-5096(99)00082-4.

[8] S. Abrate, Criteria for yielding or failure of cellular materials, J. Sandw. Struct. Mater. 10 (2008)

5–51. https://doi.org/10.1177/1099636207070997.

[9] V.S. Deshpande, N.A. Fleck, High strain rate compressive behaviour of aluminum alloy foams, Int. J. Impact Eng. 24 (2000) 277–298. https://doi.org/10.1016/S0734-743X(99)00153-0.

[10] U. Ramamurty, A. Paul, Variability in mechanical properties of a metal foam, Acta Mater. 52 (2004) 869–876. https://doi.org/10.1016/j.actamat.2003.10.021.

[11] I. Duarte, M. Vesenjak, L. Krstulović-Opara, Variation of quasi-static and dynamic compressive properties in a single aluminium foam block, Mater. Sci. Eng. A. 616 (2014) 171–182. https://doi.org/10.1016/j.msea.2014.08.002.

[12] R. Hill, ELASTIC PROPERTIES OF REINFORCED SOLIDS : SOME THEORETICAL PRINCIPLES, J. Mech. Phys. Solids. II (1963) 357–372. https://doi.org/10.1016/0022-5096(63)90036-X.

[13] E.W. Andrews, G. Gioux, P. Onck, L.J. Gibson, Size effects in ductile cellular solids. Part II: Experimental results, Int. J. Mech. Sci. 43 (2001) 701–713. https://doi.org/10.1016/S0020-7403(00)00043-6.

[14] C. Tekoğlu, L.J. Gibson, T. Pardoen, P.R. Onck, Size effects in foams: Experiments and modeling, Prog. Mater. Sci. 56 (2011) 109–138. https://doi.org/10.1016/j.pmatsci.2010.06.001.

[15] C. Redenbach, I. Shklyar, H. Andrä, Laguerre tessellations for elastic stiffness simulations of closed foams with strongly varying cell sizes, Int. J. Eng. Sci. 50 (2012) 70–78. https://doi.org/10.1016/j.ijengsci.2011.09.002.

[16] L. Li, P. Xue, Y. Chen, H.S.U. Butt, Insight into cell size effects on quasi-static and dynamic compressive properties of 3D foams, Mater. Sci. Eng. A. 636 (2015) 60–69. https://doi.org/10.1016/j.msea.2015.03.052.

[17] P. Wang, S. Xu, Z. Li, J. Yang, C. Zhang, H. Zheng, S. Hu, Experimental investigation on the strain-rate effect and inertia effect of closed-cell aluminum foam subjected to dynamic loading, Mater. Sci. Eng. A. 620 (2015) 253–261. https://doi.org/10.1016/j.msea.2014.10.026.

[18] J. Liu, S. He, H. Zhao, G. Li, M. Wang, Experimental investigation on the dynamic behaviour of metal foam: From yield to densification, Int. J. Impact Eng. 114 (2018) 69–77. https://doi.org/10.1016/j.ijimpeng.2017.12.016.

[19] Y.D. Liu, J.L. Yu, Z.J. Zheng, J.R. Li, A numerical study on the rate sensitivity of cellular metals, Int. J. Solids Struct. 46 (2009) 3988–3998. https://doi.org/10.1016/j.ijsolstr.2009.07.024.

[20] C.Y. Zhang, L.Q. Tang, B. Yang, L. Zhang, X.Q. Huang, D.N. Fang, Meso-mechanical study of collapse and fracture behaviors of closed-cell metallic foams, Comput. Mater. Sci. 79 (2013) 45–51. https://doi.org/10.1016/j.commatsci.2013.05.046.

[21] C.W. Song B, Split Hopkinson Kolsky bar: design, testing and applications., Springer, 2010.

[22] K. Kitazono, Y. Takiguchi, Strain rate sensitivity and energy absorption of Zn-22Al foams, Scr. Mater. 55 (2006) 501–504. https://doi.org/10.1016/j.scriptamat.2006.06.001.

[23] D.K. Rajak, L.A. Kumaraswamidhas, S. Das, S. Senthil Kumaran, Characterization and analysis of compression load behaviour of aluminium alloy foam under the diverse strain rate, J. Alloys Compd. 656 (2016) 218–225. https://doi.org/10.1016/j.jallcom.2015.09.255.

[24] M.A. Islam, M.A. Kader, P.J. Hazell, A.D. Brown, M. Saadatfar, M.Z. Quadir, J.P. Escobedo, Investigation of microstructural and mechanical properties of cell walls of closed-cell aluminium alloy foams, Mater. Sci. Eng. A. 666 (2016) 245–256. https://doi.org/10.1016/j.msea.2016.04.046.

[25] T. Miyoshi, M. Itoh, S. Akiyama, A. Kitahara, ALPORAS aluminum foam: Production process, properties, and applications, Adv. Eng. Mater. 2 (2000) 179–183. https://doi.org/10.1002/(SICI)1527-2648(200004)2:4<179::AID-ADEM179>3.0.CO;2-G.

[26] M. Sasso, A. Forcellese, M. Simoncini, D. Amodio, E. Mancini, High strain rate behaviour of AA7075 aluminum alloy at different initial temper states, Key Eng. Mater. 651–653 (2015) 114–119. https://doi.org/10.4028/www.scientific.net/KEM.651-653.114.

[27] L. Hua, X. Hu, X. Han, Microstructure evolution of annealed 7075 aluminum alloy and its influence on room-temperature plasticity, Mater. Des. 196 (2020) 109192. https://doi.org/10.1016/j.matdes.2020.109192.

[28] C. Mondal, A.K. Mukhopadhyay, On the nature of T(Al2Mg3Zn3) and S(Al2CuMg) phases present in as-cast and annealed 7055 aluminum alloy, Mater. Sci. Eng. A. 391 (2005) 367–376. https://doi.org/10.1016/j.msea.2004.09.013.

[29] E. Mancini, F. Campana, D. Pilone, M. Sasso, Mechanical testing of metallic foams for 3D model and simulation of cell distribution effects, Procedia Manuf. 47 (2020) 1490–1495. https://doi.org/10.1016/j.promfg.2020.04.332.

[30] E. Mancini, M. Sasso, M. Rossi, G. Chiappini, G. Newaz, D. Amodio, Design of an Innovative System for Wave Generation in Direct Tension–Compression Split Hopkinson Bar, J. Dyn. Behav. Mater. 1 (2015) 201–213. https://doi.org/10.1007/s40870-015-0019-1.

[31] M. Sasso, M.G. Antonelli, E. Mancini, M. Radoni, D. Amodio, Experimental and numerical characterization of a polymeric Hopkinson bar by DTMA, Int. J. Impact Eng. 103 (2017) 50–63. https://doi.org/10.1016/j.ijimpeng.2016.12.020.

[32] H. Kolsky, An Investigation of the Mechanical Properties of Materials at very High Rates of

Loading, Proc. Phys. Soc. Sect. B. 62 (1949) 676–700. https://doi.org/https://doi.org/10.1088/0370-1301/62/11/302.

[33] M. Bici, F. Campana, M. De Michelis, Mesoscale geometric modeling of cellular materials for finite element analysis, Comput. Aided. Des. Appl. 14 (2017) 760–769. https://doi.org/10.1080/16864360.2017.1287678.

[34] M. Bici, F. Campana, E. Mancini, D. Pilone, M. Sasso, Mesoscale modeling of aluminum foams for fea of scattering effects due to cell distribution, Comput. Aided. Des. Appl. 18 (2021) 1296–1305. https://doi.org/10.14733/cadaps.2021.1296-1305.

[35] F. Campana, D. Pilone, Effect of wall microstructure and morphometric parameters on the crush behaviour of Al alloy foams, Mater. Sci. Eng. A. 479 (2008) 58–64. https://doi.org/10.1016/j.msea.2007.06.040.

[36] F. Campana, D. Pilone, Effect of heat treatments on the mechanical behaviour of aluminium alloy foams, 60 (2009) 679–682. https://doi.org/10.1016/j.scriptamat.2008.12.045.

[37] Z. Wang, J. Shen, G. Lu, L. Zhao, Compressive behavior of closed-cell aluminum alloy foams at medium strain rates, Mater. Sci. Eng. A. 528 (2011) 2326–2330. https://doi.org/10.1016/j.msea.2010.12.059.

[38] Q.M. Li, I. Magkiriadis, J.J. Harrigan, Compressive strain at the onset of densification of cellular solids, J. Cell. Plast. 42 (2006) 371–392. https://doi.org/10.1177/0021955X06063519.

[39] Z. Li, J. Zhang, J. Fan, Z. Wang, L. Zhao, On crushing response of the three-dimensional closed-cell foam based on Voronoi model, Mech. Mater. 68 (2014) 85–94. https://doi.org/10.1016/j.mechmat.2013.08.009.

[40] Y. Sun, B. Amirrasouli, S.B. Razavi, Q.M. Li, T. Lowe, P.J. Withers, The variation in elastic modulus throughout the compression of foam materials, Acta Mater. 110 (2016) 161–174. https://doi.org/10.1016/j.actamat.2016.03.003.

[41] F. Campana, E. Mancini, D. Pilone, M. Sasso, Strain rate and density-dependent strength of AlSi7 alloy foams, Mater. Sci. Eng. A. 651 (2016) 657–667. https://doi.org/10.1016/j.msea.2015.11.007.

[42] J. Miltz, O. Ramon, Energy Absorption Characteristics of Polymeric Foams Used as Cushioning Materials, Polym. Eng. Sci. 30 (1990) 129–133.

[43] M. Avalle, G. Belingardi, R. Montanini, Characterization of polymeric structural foams under compressive impact loading by means of energy-absorption diagram, Int. J. Impact Eng. 25 (2001) 455–472. https://doi.org/10.1016/S0734-743X(00)00060-9.

[44] F. Triawan, K. Kishimoto, T. Adachi, K. Inaba, T. Nakamura, T. Hashimura, The elastic behavior of aluminum alloy foam under uniaxial loading and bending conditions, Acta Mater. 60 (2012) 3084–3093. https://doi.org/10.1016/j.actamat.2012.02.013.

[45] M. Sasso, A. Forcellese, M. Simoncini, D. Amodio, E. Mancini, High strain rate behaviour of AA7075 aluminum alloy at different initial temper states, 2015. https://doi.org/10.4028/www.scientific.net/KEM.651-653.114.

[46] R. Jhonson, C. WH, A constitutive model and data for metals subjected to large strains, high strain rates and high temperatures, Proc. 7th Int. Symp. Ballist. Hague. (1983) 541–547.

[47] M. Avalle, G. Belingardi, A. Ibba, Mechanical models of cellular solids: Parameters identification from experimental tests, Int. J. Impact Eng. 34 (2007) 3–27. https://doi.org/10.1016/j.ijimpeng.2006.06.012.

[48] Z. Nowak, R.B. Pecherski, Plastic strain in metals by shea bending. II. numerical identification and verification of plastic flwo law, Arch. Mech. 54 (2002) 621–634.

[49] K.Y. Jeong, S.S. Cheon, M.B. Munshi, A constitutive model for polyurethane foam with strain rate sensitivity, J. Mech. Sci. Technol. 26 (2012) 2033–2038. https://doi.org/10.1007/s12206-012-0509-1.

[50] K.Y. Jeong, Constitutive modeling of polymeric foams having a four-parameter modulus function with strain rate sensitivity, J. Mech. Sci. Technol. 30 (2016) 683–688. https://doi.org/10.1007/s12206-016-0124-7.